First-principles study on the electronic properties and Schottky barrier of WC/WS_2 and WC/WSe_2 heterostructures

Jiayang Wang,[1] Alexander Sredenschek,[2] David Sanchez,[1] Mauricio Terrones,[1,2,3] and Susan Sinnott[1,3,4,*]

[1]*Department of Materials Science and Engineering, The Pennsylvania State University, University Park, Pennsylvania 16802, USA*
[2]*Department of Physics, The Pennsylvania State University, University Park, Pennsylvania 16802, USA*
[3]*Materials Research Institute, The Pennsylvania State University, University Park, Pennsylvania 16802, USA*
[4]*Department of Chemistry, The Pennsylvania State University, University Park, Pennsylvania 16802, USA*

(Received 21 November 2023; revised 8 February 2024; accepted 29 March 2024; published 18 April 2024)

Within the realm of two-dimensional materials, monolayer transition metal dichalcogenide semiconductors boasting intrinsic band gaps of 1–2 eV are regarded as promising candidates for channel materials in next-generation transistors. The judicious choice of electrodes is paramount to achieving low-resistance contacts, thereby enhancing the performance of nanoelectronic devices. Therefore, the exploration of novel metal-semiconductor combinations and a comprehensive grasp of the atomistic nature of interfaces are indispensable. In this work, we present a systematic examination of vertical Moiré pattern contacts between WC and WS_2 or WSe_2, with the termination atoms (tungsten or carbon termination) being investigated through density-functional theory calculations. The Moiré pattern heterostructure is found to exhibit greater energetic favorability when compared to coherent epitaxial strain heterostructures. Our analyses encompass an in-depth exploration of the interface structure, effective potential, electron localization function, Bader charge, energy bands, and density of states within these heterostructures. These investigations reveal the formation of Schottky barriers within these systems, with the dominant carrier type and height of the Schottky barriers being under the control of the termination atoms. Metal-induced gap states formed in the interfaces give rise to a strong Fermi-level pinning. We conclude that the WC/WSe_2 heterostructure with carbon terminations in WC have the smallest *p*-type Schottky-barrier height of 0.08 eV among all other heterostructures considered. Transport properties are assessed using the Simmons tunneling injection model. These findings yield valuable insights that can be leveraged in the design of high-performance nanoelectronic d built upon two-dimensional materials.

DOI: 10.1103/PhysRevMaterials.8.044004

I. INTRODUCTION

Since the successful synthesis of single-layer graphene in 2004 [1], two-dimensional (2D) materials have received significant attention due to their unique mechanical, electrical, and optical properties, offering the possibility of creating novel materials with specific structure-property relationships [2–8]. Atomically thin films of 2D materials are composed of a monolayer or a few atomic or molecular layers. While the intralayer bonding consists of covalent bonds, ionic bonds, or a combination of these, the interlayers are bonded by weaker van der Waals interactions. Transition metal dichalcogenides (TMDs) can be potentially used as next-generation channel materials in field-effect transistors (FETs). In TMD-based FET devices, the metallic electrodes are selected or functionalized to modify the chemical reactivity of the TMD layers, further tuning the electronic structures of the contact region. Furthermore, the formation of a Schottky barrier between the electrode and the TMD is a significant challenge to overcome [9]. This barrier, characterized by a finite Schottky-barrier height (SBH) can impede the charge injection, leading to the degradation of device performance. As a result, the imperative task at hand is to exert controllable SBH contact or Ohmic contact at metal/semiconductor interfaces. This involves the selection of proper metal electrodes and optimization of the contact interface to enhance the inherent transport properties of channel materials and improve the device performances [10].

MXenes are a class of 2D materials composed of transition metal carbides, nitrides, and carbonitrides and their properties can be modified by compositions and surface functional groups. MXenes are being considered for use in lithium batteries due to their excellent properties, including high electrical capacities and conductivity [11], which also make them suitable for FET electrodes. Metals containing *d*-orbital electrons are suitable for electrodes due to the overlap with *d*-orbital electrons in TMDs, resulting in better injection of the electron wave vector. In addition, compared with pure metal, the MXenes have the advantage of tunable work function [12] and good mechanical properties. Xu *et al.* [13] applied $Ti_2C(OH)_xF_y$ MXenes as electrodes into *n*-type MoS_2 and *p*-type WSe_2 FET and they found low SBH, which indicated a promising candidate for 2D electrodes in complementary metal-oxide-semiconductor inverters. Peng *et al.* [14] computationally investigated the interfacial properties between Nb_2CT_2 (T = OH, F, O) and MoS_2 to reveal the effect of surface functionals and electrical field on the

*Corresponding author: sinnott@matse.psu.edu

SBH, which originated from the tunable work function of MXenes. Li *et al.* [15] explored the electrical contact type of heterostructures between WS_2 and Nb_2CX_2 (X = H, F, Cl) for both vertical and lateral types and they found the Ohmic and n-type Schottky contact occurred with different X and orientations. Li *et al.* [16] studied the interfacial properties of WS_2 and MXenes (Ti_2C, V_2C, Cr_2C, Hf_3C, and Ti_3C) using first-principles calculations. They found Ohmic contact for vertical heterostructures and small SBH for lateral heterostructures, indicating an ideal electrode for WS_2 to generate transistors.

Two potential routes could be implemented to experimentally realize the TMC/TMD heterostructures, and they involve either mechanically transferring or chemically converting the parent materials. A bottom-up chemical vapor deposition (CVD) synthesis method has been reported to prepare nonlayered, ultrathin transition metal carbides (TMC) such as molybdenum, tungsten, and tantalum carbide (α-Mo_2C, WC, and TaC) [17]. Wet chemical transfer of α-Mo_2C and MoS_2 has been implemented to synthesize α-Mo_2C/MoS_2 vertical heterostructures for photodetection [18]. While this mechanical method has the potential to control the twist angle between the materials, the cleanliness of the transfer method may impact the contact formed at the interface. Chemical conversion involves either carburization or chalcogenization of the parent materials. Jeon and Choi *et al.* [19,20] implemented a methane carburization to partially convert mechanically exfoliated and CVD-grown MoS_2 into Mo_2C. The resulting epitaxial, lateral heterostructures exhibited a reduced contact resistance due to the formation of an atomically sharp metal-semiconductor interface. Another route based on partial sulfurization of the as-grown carbides led to α-Mo_2C/MoS_2 vertical heterostructures with novel transport properties [21,22].

As of now, very few studies were considering tungsten carbide based Schottky contact in FET although they have revealed outstanding properties and can be good candidates for catalysts [23–28]. Fiori *et al.* [29] synthesized the WC/p-type diamond heterojunction and studied the Schottky-barrier interface, from which the rectification abilities can be attained at high temperatures (800 K). Hu *et al.* [30] computationally investigated the interface between WC and diamond and excellent rectifying behavior was justified. Enlightened by unique properties and experimental capabilities of synthesis, it would be naturally interesting to explore the possible usage of WC as an electrode in TMD-based FET. In this work, we investigate the contact type and SBH of WC/WS_2 and WC/WSe_2 heterostructures using first-principles methods.

II. COMPUTATIONAL METHODS

All the first-principles calculations were carried out using the Vienna *ab initio* simulation package (VASP) [31], which implements density-functional theory (DFT) and a plane-wave basis set with the projector-augmented wave method [32]. The exchange-correlation functions are approximated through generalized gradient approximation as stated in Perdew-Burke-Ernzerhof parametrization [33]. The plane-wave cutoff energy was set to 500 eV and the Monkhorst-Pack k mesh was sampled with a density of 0.05 $Å^{-1}$. As for structure relaxation, the thresholds for determination of convergence were using 10^{-5} eV as energy break conditions for the electronic self-consistence loop and Hellmann-Feynman force on each atom is less than 0.01 eV/Å. For the Moiré pattern heterostructures, the nonlocal vdW-DF-optB88 exchange-correlation functional [34] was applied to describe the dispersion interaction within the interface. For all the 2D structures, a 15 Å thickness of vacuum layer was used to eliminate interaction between neighboring supercells due to the periodic boundary conditions. Bader charge analysis was used to calculate the charge transfer between the TMD slab and the TMC slab. Furthermore, a recompiled VASP version that is suitable for 2D structure relaxation was used, which fixed the length of the supercell of the c direction. For Moiré pattern interface design, supercells of TMD and TMC slabs are aligned in large supercell sizes to minimize the lattice mismatch. The Moiré pattern builder that was implemented in the VASPKIT [35] program was used to generate heterostructures with limited in-plane strain (0.15%).

TABLE I. Lattice constants and band gaps of WS_2, and WSe_2, and WC; a and d are the lattice constants along the a and c directions, l is the bond length between tungsten and carbon or chalcogen atoms.

	a (Å)	d (Å)	L (Å)	E_g (eV)
δ-WC	2.926	2.841	2.205	
WS_2	3.189	3.155	2.424	1.81
WSe_2	3.323	3.354	2.548	1.54

III. RESULTS AND DISCUSSION

Tungsten carbide, specifically the δ phase with a $P\bar{6}m2$ space group, were used to construct vertical heterostructures with monolayer WS_2 (ML-WS_2) or ML-WSe_2. This choice was informed by the phase diagram [36], indicating that the δ phase is the most stable and can be readily synthesized via the CVD method [17,37]. Notably, prior theoretical investigations have indicated that the [0001] phase of δ-WC with a W termination exhibits the lowest surface energy when compared to other low-index orientations [38]. Both ML-WS_2 and ML-WSe_2 adopt the 1H crystal structure, where tungsten atoms occupy trigonal prismatic sites formed by chalcogen atoms. Figure 1 presents the atomic structures and electronic structures of WC, WS_2, and WSe_2. Each component was independently subjected to full relaxation, resulting in monolayer TMDs with direct band gap. The lattice parameters and band-gap values are provided in Table I. Drawing upon previous experiments that have validated the possibility of forming vertical heterostructures between [0001] γ-MoC and [0001] MoS_2 [21], it is worth noting that DFT energy calculations have further indicated the energetic feasibility of both Mo-termination and C-termination heterostructures. These findings have been corroborated through cross-sectional Transmission Electron Microscopy (TEM) imaging [21]. In this work, we will focus on the systems involving tungsten carbide with sulfur and selenium as the chalcogen atoms. δ-WC, WS_2, and WSe_2 adopt hexagonal arrangements, but they significantly differ in terms of lattice constants. To assess this lattice mismatch, we apply the formula $\Delta a/a = (a_{TMD} - a_{TMC})/\, a_{TMD}$, in which a_{TMD} denotes

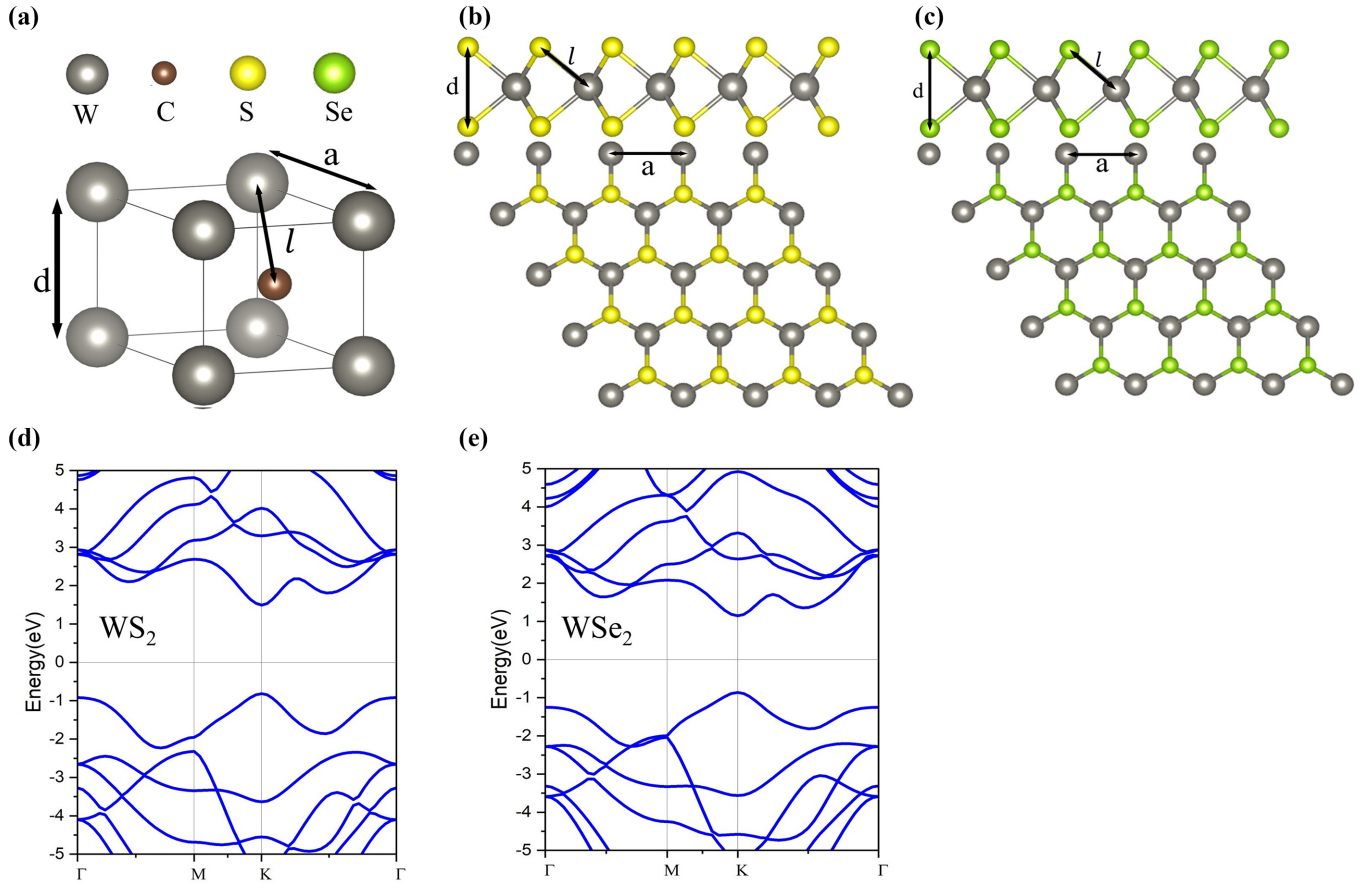

FIG. 1. Atomic structure of (a) δ-WC. (b) Side view and top view of (b) ML-WS_2 and (c) ML-WSe_2. The band structure of (d) ML-WS_2 and (e) ML-WSe_2.

the lattice parameter of the TMD, and a_{TMC} corresponds to the tungsten carbide's lattice parameter. Based on Table I, there is an 8.99% lattice mismatch observed between WC/WS_2 and a 13.57% mismatch for WC/WSe_2. The creation of coherent epitaxial strain heterostructures results in substantial in-plane tensile strain in WC and compressive strain in the TMDs. However, the energy reduction resulting from interface formation does not offset the energy increase due to in-plane strain. The quantitative comparison between the formation enthalpy of coherent epitaxial heterostructures and Moiré heterostructures will be discussed.

Vertical heterostructures are constructed by layering $m-WS_2$ or $m-WSe_2$ atop a nine-atomic-layered WC. We note that a nine-layer slab is considered sufficiently thick to eliminate interactions between the upper and lower surfaces [38]. Additionally, given the polar nature of the [0001] tungsten carbide surface, both W termination and C termination have been considered, and they are denoted as WC-*m* and WC-*c*, respectively. Two types of heterostructures are compared. For coherent epitaxial strain heterostructures, as depicted in Figs. 2(a) and 2(b), the size of the supercell is $2 \times 2 \times 1$ and the thickness of vacuum space is 18 Å to eliminate interaction between nearby supercells. Figures 2(a) and 2(b) represent AB and AA stacking of WC-*m*/WS_2, respectively. In AB stacking, the interfacial atom of WC is directly beneath the center of the hexagonal ring of $WS(Se)_2$, while in AA stacking, the interfacial atom of WC is directly beneath the sulfur (selenium) atoms of $WS(Se)_2$. Figures 2(a) and 2(b) are representative configurations, and similar models are built and calculated for WC-*c*/WS_2, WC-*c*/WSe_2, and WC-*m*/WSe_2 (those structures are not shown here). On the other hand, for Moiré pattern heterostructures, as depicted in Figs. 2(d)–2(g), which stand for four systems: WC-*c*/WS_2, WC-*m*/WS_2, WC-*c*/WSe_2, and WC-*m*/WSe_2. The sizes of supercells for Moiré patterns are varied depending on the lattice mismatch between WC/$WS(Se)_2$ and vacuum levels are kept the same as their coherent epitaxial strain counterparts. In order to mitigate the influence of in-plane strain on the electronic structure and to provide clearer insights into the interfacial properties, the Moiré pattern heterostructures are characterized by minimal in-plane strain (<0.15%). Figure 2(c) schematically shows the configuration of coherent epitaxial heterostructures and Moiré pattern heterostructures. In the left figure, the atomic alignment between two layers results in greater orbital overlap and lower interlayer distance, while for Moiré pattern heterostructures, the lattice mismatch prevents a large orbital overlap. Table II quantitatively summarizes and compares the geometry and energy information of coherent epitaxial and Moiré pattern heterostructures. The coherent epitaxial heterostructures generally have a smaller interlayer distance compared to their Moiré pattern counterparts, which leads to a greater work of adhesion. However, comparing the energy, Moiré pattern heterostructures generally have a lower heat of formation than that of coherent epitaxial heterostructures. For

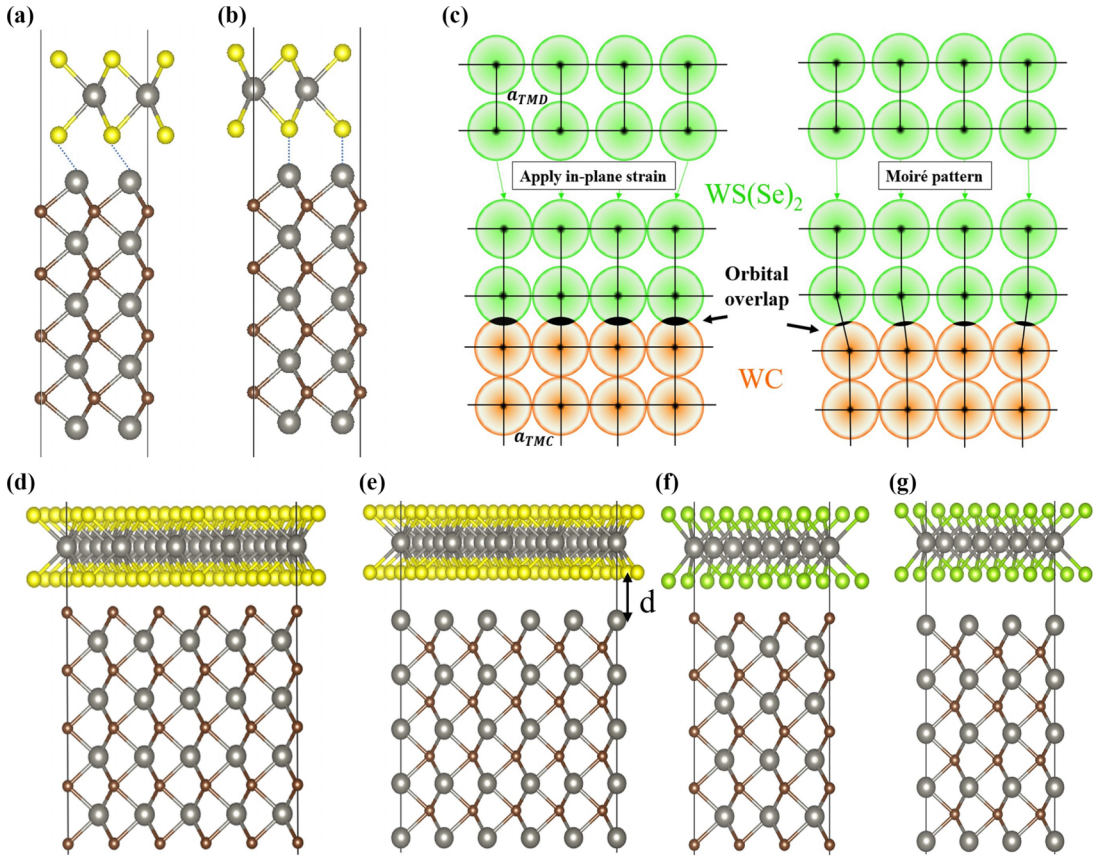

FIG. 2. WC-*m*/WS_2 coherent epitaxial strain heterostructures with AB stacking (a) and AA stacking (b). (c) Schematics showing the impact of lattice mismatch to the interface: coherent lattice constant maximizes the orbital overlap (left) while Moiré pattern prevents maximizing orbital overlap (right). Side view of Moiré pattern heterostructure: (d) WC-*c*/WS_2; (e) WC-*m*/WS_2; (f) WC-*c*/WSe_2; (g) WC-*m*/WSe_2.

example, in WC-*m*/WS_2, the heat of formation of the Moiré pattern heterostructure is approximately five times smaller than that of the coherent epitaxial heterostructures. Due to the large in-plane strain, the overall formation energies of coherent epitaxial heterostructures are risen so that the Moiré pattern heterostructures become energetically more favorable. The positive values of heat of formation in Table II are due to the existence of tungsten carbide surface and will not influence the comparison. Hence, the following study will be focused on Moiré pattern heterostructures. Comprehensive structural details of the Moiré pattern heterostructures followed by full relaxation can be found in Table III. For WC-*c*/WS_2 and WC-*m*/WS_2, 5×5 WC matches $\sqrt{21} \times \sqrt{21}$ WS_2 with twist angle 10.89°; for WC-*c*/WSe_2 and WC-*m*/WSe_2, 3×3 WC matches $\sqrt{7} \times \sqrt{7}$ WSe_2 with twist angle 19.11°. This set of combinations allows very small in-plane strain after relaxation. For WC, almost 0 in-plane strain is applied and the maximum strain on $WS(Se)_2$ is less than 0.15%.

To confirm the stability of the interface between the TMD and TMC, we have performed calculations on both the work of adhesion and interfacial energy. The work of adhesion quantifies the energy needed to separate the adherent interface and create two distinct surfaces. It can be determined using Eq. (1):

$$W_{\text{ad}} = \frac{E_{\text{TMC}} + E_{\text{TMD}} - E_{\text{heterostructure}}}{S_{\text{area}}}, \tag{1}$$

where W_{ad} is the work of adhesion in units of J/m^2; E_{TMC}, E_{TMD}, and $E_{\text{heterostructure}}$ are the total energies of the WC thin film, the WS_2 or WSe_2 monolayer, and the WC/$WS(Se)_2$ heterostructure, respectively; and S_{area} is the interfacial area of the heterostructure.

TABLE II. Summary of geometric and energetic information of coherent epitaxial strain heterostructures and Moiré pattern heterostructures; AB and AA stacking correspond to Figs. 3(a) and 3(b); Moiré stands for Moiré pattern heterostructures that are depicted in Figs. 3(d)–3(g).

	WC-*c*/WS_2			WC-*m*/WS_2			WC-*c*/WSe_2			WC-*m*/WSe_2		
	AB	AA	Moiré	AB	AA	Moiré	AB	AA	Moiré	AB	AA	Moiré
Interlayer distance (Å)	2.24	1.92	2.40	2.26	2.37	2.51	2.58	2.04	2.78	2.25	2.44	2.69
Heat of formation (eV/atom)	0.145	0.160	0.077	0.105	0.098	0.022	0.156	0.209	0.074	0.167	0.120	0.025

TABLE III. Geometric information of heterostructures; size is the number of lattices of WC and $WS(Se)_2$ along x-y plane for building up the supercell; twist angle is the relative rotation angle between WC and $WS(Se)_2$; d is interlayer distance between TMC and TMD.

			In-plane strain (%)		d (Å)
	Size (TMC, TMD)	Twist angle	TMC	TMD	
WC-*c*/WSe_2	5×5, $\sqrt{21} \times \sqrt{21}$	10.89°	+0.002	+0.11	2.40
WC-*m*/WS_2					2.51
WC-*c*/WSe_2	3×3, $\sqrt{7} \times \sqrt{7}$	19.11°	+0.002	−0.15	2.78
WC-*m*/WSe_2					2.69

The interfacial energy is characterized as the energy necessary for the creation of an interface from bulk materials. This value can be obtained through Eq. (2):

$$\gamma_{\text{int}} = \sigma_{\text{TMC}} + \sigma_{\text{TMD}} - W_{\text{ad}}, \tag{2}$$

where σ_{TMC} and σ_{TMD} are the surface energy of WC and $WS(Se)_2$, respectively, and W_{ad} is the work of adhesion defined by Eq. (1).

It is to be noted that WC will produce a polar surface on the [0001] facet, resulting in a substoichiometric atomic ratio in the WC slab model. In such instances, the equation used to compute surface energy is as follows [39]:

$$\sigma_{\text{WC}} = \frac{1}{2A}\left[E_{\text{slab}}^{\text{WC}} - N_{\text{W}}\mu_{\text{bulk}}^{\text{WC}} + (N_{\text{W}} - N_{\text{C}})\mu_{\text{bulk}}^{\text{C}} + (N_{\text{W}} - N_{\text{C}})\Delta\mu_{\text{C}}\right], \tag{3}$$

where A is the surface area; $E_{\text{slab}}^{\text{WC}}$, $\mu_{\text{bulk}}^{\text{WC}}$, and $\mu_{\text{bulk}}^{\text{C}}$ are the total energy of the WC slab model, WC bulk, and carbon in graphite, respectively. $\Delta\mu_{\text{C}}$ represents the chemical potential difference between the carbon-deficient condition and carbon-rich condition (in graphite). N_{W} and N_{C} are the number of tungsten and carbon atoms in the slab model, respectively. Hence, as for a polar surface, the surface energy is a range based on the chemical potential of carbon. For simplicity, we fix the chemical potential of carbon equal to the energy of carbon from graphite, i.e., $\Delta\mu_{\text{C}} = 0$. The surface energies of WC-[0001] are 5.51 and 3.66 J/m^2 for carbon termination and tungsten termination, respectively, which is consistent with previous work [30]. The surface energies of WS_2 and WSe_2 [0001] is 0.34 and 0.45 J/m^2, respectively, which is a typical van der Waals effect [40]. The work of adhesion and interfacial energies of four types of heterostructures are summarized in Table IV. The results clearly show that the surface energy of WC with a W termination is lower than that with a C termination, signifying that the W-terminated surface is the more energetically favorable option. This surface energy value aligns with previous computational findings [41]. The work of adhesion serves as an indicator of the binding strength at the interface. The magnitude of the work of adhesion is comparable to but slightly higher than typical van der Waals forces (0.2–0.5 J/m^2 [40]) by about 0.2 J/m^2, suggesting that the interfaces are predominantly governed by van der Waals interactions but hybrid with a small portion of strong bond characteristics. The W termination exhibits a stronger binding energy than the C termination for both WS_2 and WSe_2. The interfacial energy directly correlates with relative stability; a lower interfacial energy signifies a more stable configuration. Consequently, the W termination is confirmed to be the energetically preferred choice.

TABLE IV. The work of adhesion and interfacial energies of four TMC/TMD heterostructures.

Heterostructures	Work of adhesion (J/m^2)	Interfacial energy (J/m^2)
WC-*c*/WS_2	0.37	5.48
WC-*m*/WS_2	0.76	3.24
WC-*c*/WSe_2	0.3	5.55
WC-*m*/WSe_2	0.73	3.38

IV. ELECTRONIC PROPERTIES

To explore the interfacial characteristics of TMC/TMD heterostructures, we have conducted calculations for the tunneling barrier height (TBH), Bader charge analyses, and Schottky-barrier height. The tunneling barrier serves as a metric for assessing the efficiency of carrier injection in the heterojunction, and it can be extracted from the effective potential curve (V_{eff}). V_{eff} delineates the interaction of a single electron with other electrons and the nuclei. This V_{eff} value can be determined using the following equation [9]:

$$V_{\text{eff}} = V_{\text{xc}} + V_{\text{H}} + V_{\text{ext}}, \tag{4}$$

where the three terms on the right-hand side correspond to exchange-correlation potentials, Hartree potentials, and electrons-nuclei interaction, respectively. In Fig. 3, the average effective potential along the z direction traversing the interface is plotted for all four heterostructures. The TBH, denoted as Φ_{TB}, represents the potential energy greater than Fermi level at the metal-semiconductor interlayer vacuum. It can be defined as the energy difference between the WC/$WS(Se)_2$ gap and Fermi level. The barrier mainly comes from the interface dipole [42]. Φ_{TB} can be computed using the following equation:

$$\Phi_{\text{TB}} = V_{\text{gap}} - E_f. \tag{5}$$

V_{gap} is the potential barrier within the WC/$WS(Se)_2$ interface and E_f is the Fermi level of the heterostructures. A lower TBH indicates a more efficient electron injection. Based on Fig. 3, the TBHs of metal-terminated heterostructures are generally lower than that of carbon termination. The TBHs of WC-*c*/WS_2, WC-*m*/WS_2, WC-*c*/WSe_2, and WC-*m*/WSe_2 are 5.82, 2.46, 6.34, and 1.31 eV, respectively. These barriers are much

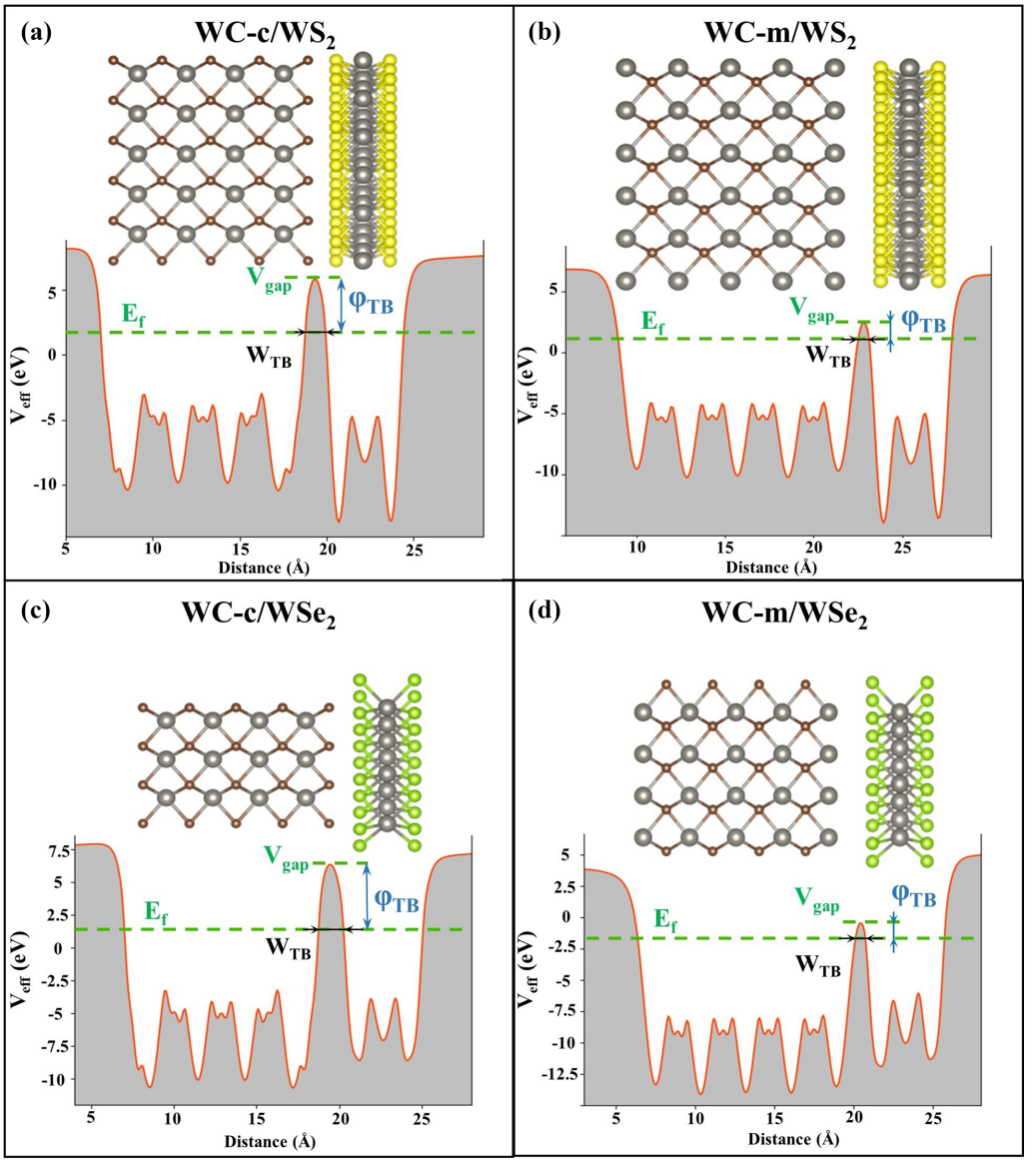

FIG. 3. Average effective potentials along the z direction for (a) WC-c/WS_2; (b) WC-m/WS_2; (c) WC-c/WSe_2; (d) WC-m/WSe_2.

lower than Au-WSe_2 [9] and comparable to Nb_2C/WS_2 [15]. The widths of tunneling barrier W_{TB} are also shown in Fig. 3. It is worth noting that the widths of the interfacial potential peaks, closely linked to interfacial distances, follow the same trend as the tunneling barrier height. Specifically, WSe_2 exhibits the lowest TBH when in contact with metal-terminated WC, suggesting superior carrier tunneling transmission efficiency.

The tunneling-specific resistivity (ρ_t) can be determined using the calculated tunneling barrier and barrier width [43,44]. Following the Simmons tunneling injection model [45], we compute the ρ_t using the following equation:

$$\rho_t \approx \frac{8\pi^2 W \alpha \hbar^2}{3e^2\sqrt{2m_e\Phi_{TB}}}\, e^{2W\sqrt{2m_e\Phi_{TB}}/\hbar}, \tag{6}$$

where $\hbar$ and m_e are the reduced Planck constant and mass of the free electron, W is the width of the tunneling barrier estimated with respect to Fermi level, and the value of α is 1 under the square-barrier approximation. The calculated ρ_t values are summarized in Table V. For carbon termination, the ρ_t is comparable to other similar systems, such as Bi/Sb-TMD ($1.49 \times 10^{-9} - 6.17 \times 10^{-9}\,\Omega\,cm^2$) [46] and MSi_2N_4/XY_2 (X = Nb, Ta; Y = S, Se, Te) ($2.79 \times 10^{-9} - 4.79 \times 10^{-9}\,\Omega\,cm^2$) [47]. For metal termination, the ultralow ρ_t indicate the significant efficiency or carrier tunneling injection, suggesting potential applications in high-performance devices. The calculated ρ_t

TABLE V. The tunneling barrier height and width of WC/$WS(Se)_2$ interfacial potential barrier. Tunneling-specific resistivity in the unit of $10^{-9}\,\Omega\,cm^2$.

	WC-c/WS_2	WC-m/WSe_2	WC-c/WSe_2	WC-m/WSe_2
Φ_{TB} (eV)	5.82	2.46	6.34	1.31
W_{TB} (Å)	1.89	1.09	2.06	0.94
ρ_t ($\Omega\,cm^2$)	5.29	0.25	10.50	0.16

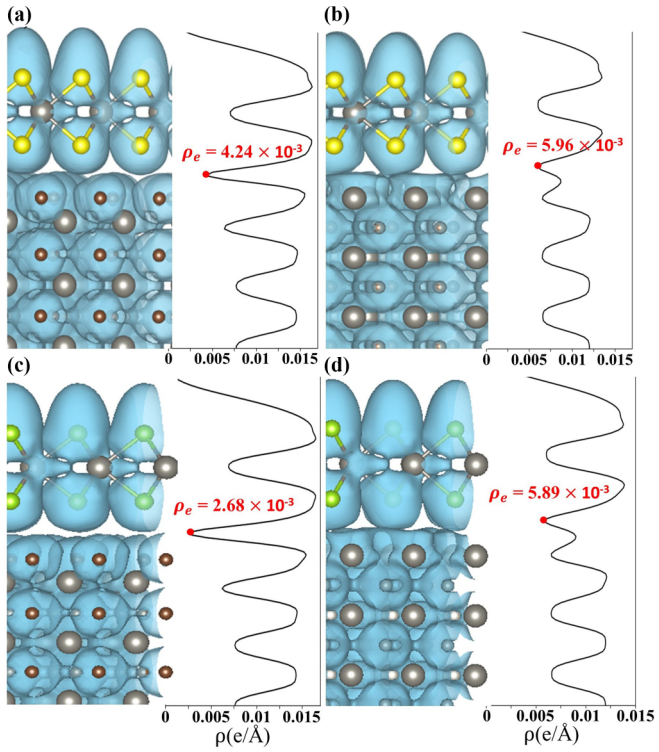

FIG. 4. Electron localization functions and electron densities for (a) WC-*c*/WS_2; (b) WC-*m*/WS_2; (c) WC-*c*/WSe_2; (d) WC-*m*/WSe_2.

can be employed to analyze the contact resistance and transport measurement of the devices.

To further delve into the atomic orbital overlap at the WC/$WS(Se)_2$ interface, we have visualized the electron densities and electron localization functions, as presented in Fig. 4. In these visualizations, the isosurface is consistently set to $0.3e/Å^3$. Additionally, we have determined the minimum values of the $x-y$ plane-averaged electron density (ρ_e) at the interface. In Figs. 4(a) and 4(c), the carbon-terminated interfaces display relatively low ρ_e values, suggesting weak atomic orbital overlap and interfacial interactions. On the other hand, the tungsten-terminated interfaces exhibit stronger atomic orbital overlap and interfacial interactions, which can result in low-resistance contacts. These findings align with previous assessments of adhesion and tunneling barrier calculations.

Building upon the preceding energy calculations, the interfacial bonding encompasses a component of strong chemical bonding. This situation can lead to charge transfer and redistribution occurring within the interface. At WC/$WS(Se)_2$ interfaces, charge redistribution plays a pivotal role in the formation of an interface dipole. This dipole can shift the electronic levels from their original positions, leading to a deviation in SBH from the Schottky-Mott limit. The charge redistribution at the contact interface can be effectively characterized using the charge density difference ($\Delta\rho$), which is defined as

$$\Delta\rho = \rho_{\mathrm{WC/WS(Se)_2}} - \rho_{\mathrm{WC}} - \rho_{\mathrm{WS(Se)_2}}, \tag{7}$$

where the three terms on the right-hand side represent the charge densities of the WC/$WS(Se)_2$ heterostructures, the WC layers, and the $WS(Se)_2$ layers, respectively. The charge density differences are graphically presented in Fig. 5, with pink indicating electron accumulation and cyan signifying electron depletion. The isosurface is consistently set at $3.3 \times 10^{-3} e/Å^2$. Notably, the charge accumulation and depletion are evident at the interface, indicating the formation of interfacial dipoles. It is important to note that the direction and magnitude of charge transfer vary across each heterostructure. To quantify this charge transfer, Bader charge analyses have been applied, as depicted in Fig. 5. In the case of the Moiré pattern, each atom at the interface resides in a slightly different chemical environment, leading to slight variations in Bader charges within the same layers. Consequently, the charge of each atom is considered as the average value for the entire layer. For the carbon termination, it is observed that a negligible amount of charge transfer occurs from $WS(Se)_2$ to WC, amounting to approximately $0.06 - 0.08e$. In contrast, for metal termination, the charge transfer is more substantial and occurs in the opposite direction, from WC to $WS(Se)_2$, with a magnitude of approximately $0.21e$. This suggests that the metal termination cases exhibit stronger interactions within the interface and a greater interfacial dipole.

For a more comprehensive insight into the electronic structures and transport properties, we have calculated SBH. Two DFT methods are commonly used, based on projected band structure and based on Schottky-Mott rule. Previous study shows that two methods provide similar results [48], thus we will use projected band structures for WC/$WS(Se)_2$ heterostructures. As displayed in Fig. 6, the gray lines represent the energy bands of the entire heterostructures, while the "fat band" filled with orange color signifies the contributions from WS_2 or WSe_2. We have observed that the WC and TMD are slightly hybridized but the band structures of WS_2 and WSe_2 remain identifiable, with the band gap retained. This preservation can be attributed to the weak van der Waals effect and the limited extent of charge transfer across the interface, preventing full metallization of the semiconductors. There are small amounts of spilled states within the band gap of WS_2 and WSe_2, which are recognized as MIGS. These states will be further discussed in a later analysis. It is noteworthy that the position of the Fermi level varies among different heterostructures. When WC is carbon terminated, the Fermi level of heterostructure is closer to the valence band maximum (VBM) than to the conduction band minimum (CBM), indicating the semiconductors are *p*-type doped and resulting in a *p*-type Schottky barrier. Conversely, when WC is metal terminated, the Fermi level is closer to the CBM, indicating *n*-type doping in semiconductors and resulting in an *n*-type Schottky barrier. This finding can be explained by the results from Bader charge analyses that the direction and the amount of charge transfer determine the types of Schottky barrier [9,49].

To further quantitatively assess the SBH, we have generated a partial density of states (pDOS), as illustrated in Fig. 7. The Fermi level is set to 0 eV. The yellow shade depicts the gap between the Fermi level and the VBM, and the green shade represents the gap between the CBM and the Fermi level. The pDOS within the gap is quite low, which could be reasonably regarded as MIGS [50,51]. The width of the yellow or green regions estimates the SBH. For carbon-terminated heterostructures, WC-*c*/WS_2 and WC-*c*/WSe_2, the *p*-type SBHs are 0.24 and 0.08 eV, and the electron SBHs

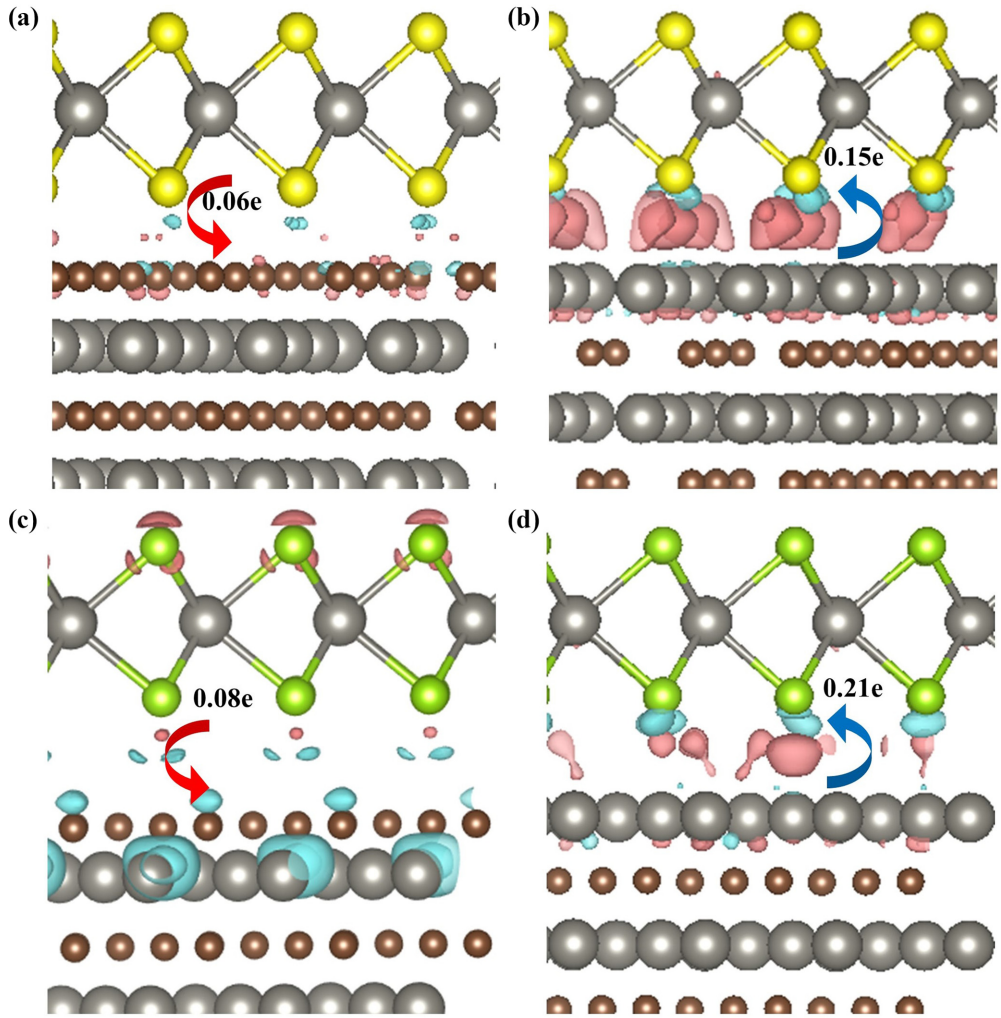

FIG. 5. Charge density difference of heterostructures for (a) WC-*c*/WS_2; (b) WC-*m*/WS_2; (c) WC-*c*/WSe_2; (d) WC-*m*/WSe_2. The pink and cyan stand for electron accumulation and depletion, respectively. The isosurface level is $3.3 \times 10^{-3} e/\text{Å}^2$.

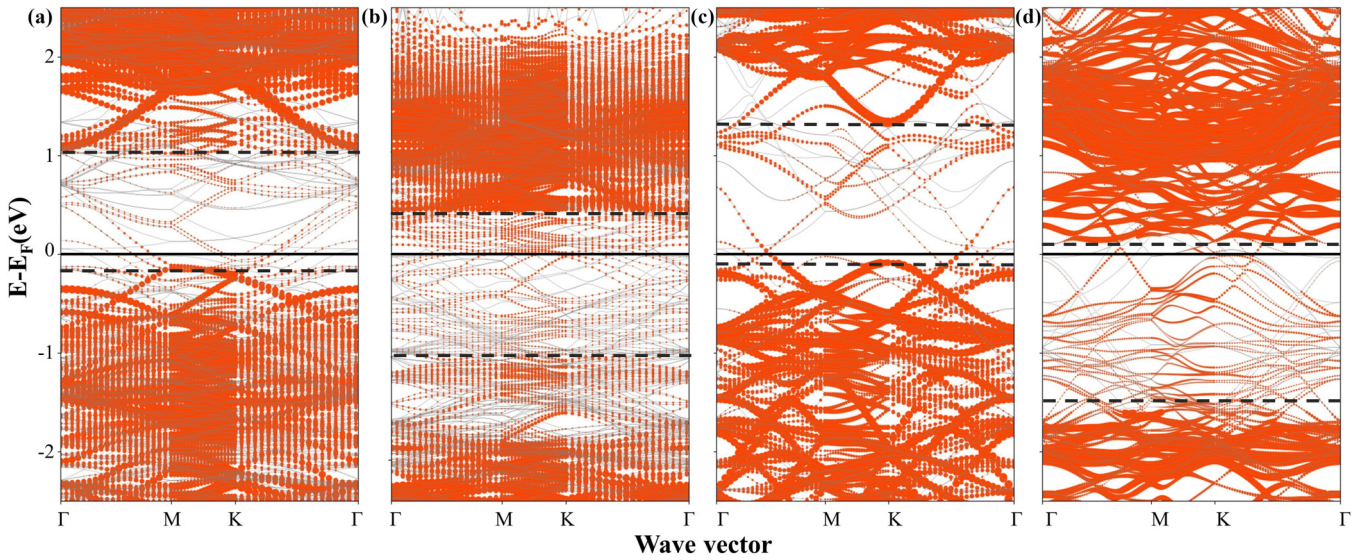

FIG. 6. The projected band structure of (a) WC-*c*/WS_2; (b) WC-*m*/WS_2; (c) WC-*c*/WSe_2; WC-*m*/WSe_2. The black lines standing for Fermi levels are set to zero. The gray curves are bands of whole heterostructures, the orange shaded "fat bands" represent the contributions from WS_2 or WSe_2, and the width of the line is proportional to the band's weight. The black dashed lines represent the CBM and VBM of heterostructures.

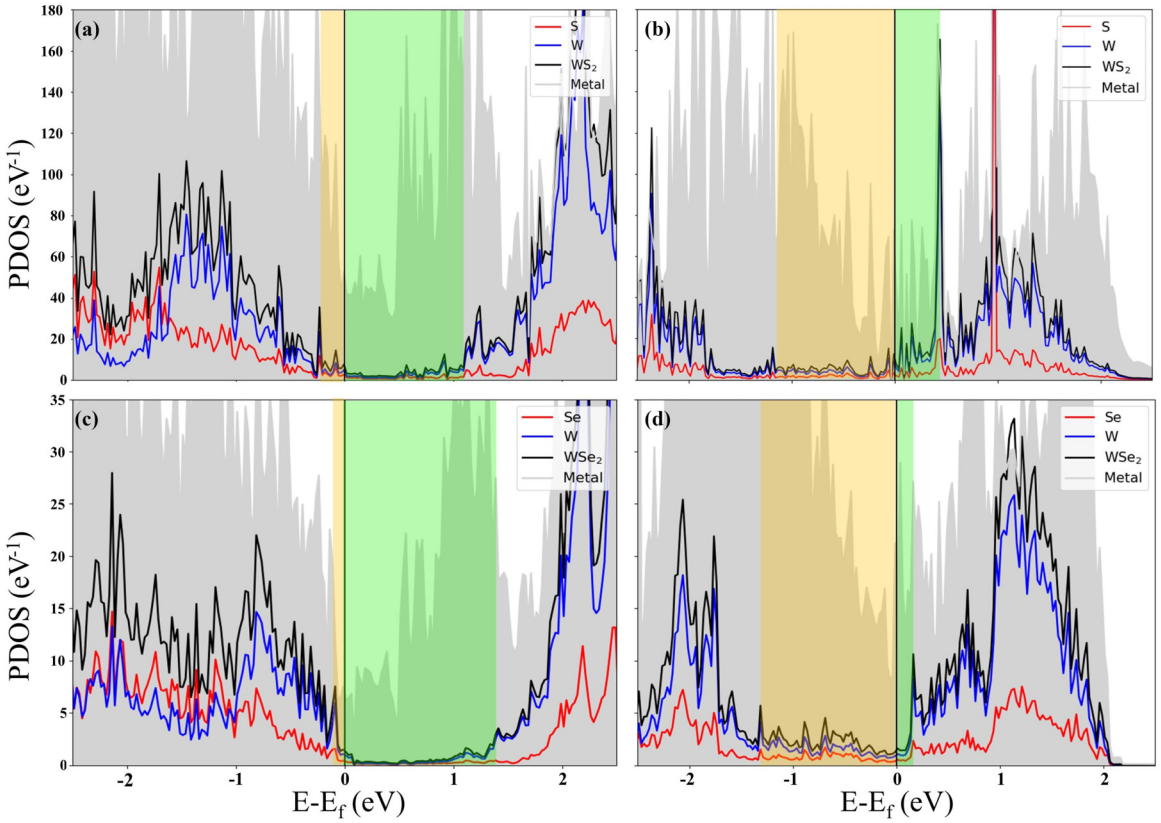

FIG. 7. The partial density of states of (a) WC-*c*/WS_2; (b) WC-*m*/WS_2; (c) WC-*c*/WSe_2; (d) WC-*m*/WSe_2. Fermi level is set to zero. The red, blue, and black curves represent the density of states of sulfur, tungsten in semiconductor, and their summation; the gray shade stands for the metal density of states. The yellow region is the gap between VBM and Fermi level, indicating hole SBH; the green region is the gap between CBM and Fermi level describing electron SBH.

are 1.08 and 1.39 eV. In contrast, the metal-terminated heterostructures, WC-*m*/WS_2 and WC-*m*/WSe_2, form *n*-type SBHs of 0.45 and 0.13 eV, and hole SBHs are 1.12 and 1.34 eV.

The electron SBH results were compared with other references and summarized in a scatter plot in Fig. 8. The blue color denotes the metal/WS_2 heterostructures, while the red hue stands for the metal/WSe_2 heterostructures. Abstracted from various references, data points are represented by square [16], star [51], triangle [52], and plus [9] shapes, while the empty circles denote the calculations in this work. Data points located at 0 SBH indicate the formation of Ohmic contact and full metallization of semiconductors. All of them are vertical heterostructures. It can be found that the electron SBH values vary in a relatively narrow range (0–1.39 eV) comparing to the work function of the metal surface (2.78–6.49 eV), which indicate the existence of the FLP effect in WS_2 and WSe_2 contact. To quantitatively evaluate the FLP effect, the pinning factor *S* is calculated as

$$S_{n/p} = \frac{\partial \mathrm{SBH}_{n/p}}{\partial \mathrm{WF}}. \tag{8}$$

$\mathrm{SBH}_{n/p}$ is *n*- or *p*-type SBH of a semiconductor and WF is the work function of a metal surface. This equation can be used to evaluate the ability of a semiconductor surface to screen out the influence of metal [53]. According to the

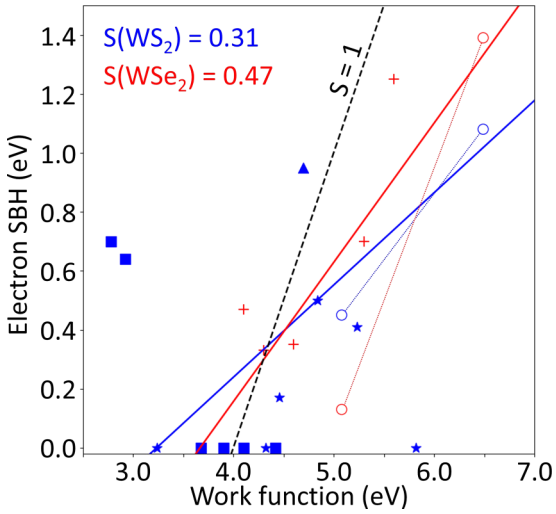

FIG. 8. The data summary of vertical SBH as a function of the work function of metals. The blue and red colors represent metal/WS_2 heterostructures and metal/WSe_2 heterostructures, respectively. The square [16], star [51], triangle [52], and plus [9] data points are abstracted from references; the empty circles denote the calculations in this work. The blue and red lines depict the slope parameter for WS_2 and WSe_2, respectively. The black dashed line represents the $S = 1$ for comparison.

TABLE VI. The Schottky-Mott limit SBH is calculated through Schottky-Mott rule.

Heterostructure	WC-*c*/WS_2	WC-*m*/WS_2	WC-*c*/WSe_2	WC-*m*/WSe_2
Schottky-Mott Limit SBH (eV)	2.1	0.69	2.43	1.02

definition, $S = 1$ represents no FLP and $S = 0$ represents complete FLP. In determining the slope parameters depicted in Fig. 8, we exclude the data points where the SBH equals zero, representing Ohmic contact due to the full metallization of WS_2. Additionally, we disregard the two leftmost two square dots (with work function ranging from 2.78 to 2.92 eV) showing anomalously high SBH, as previous research suggests that they cannot be predicted through metal's work function [16]. The remaining data points, combined with this work, are linearly fitted, yielding slope parameters of 0.31 for WS_2 and 0.47 for WSe_2. These results are slightly larger than previous experimental measurements [54] and theoretical results [55]. The black dashed line represents $S = 1$ for comparison. Interestingly, the blue and red dotted lines denote the slope parameters of WS_2 and WSe_2 specifically obtained from this study, which are 0.45 and 0.89, respectively, larger than the references. This discrepancy can be attributed to the presence of Moiré pattern heterostructures, resulting in a larger interlayer distance compared to coherent epitaxial strain heterostructures, as illustrated in Fig. 2(c) and calculated in Table II. The lattice mismatch arising from the Moiré pattern hinders the orbital overlap between interfacial atoms, thereby weakening the interfacial interaction between metal and TMD and leading to a weaker FLP. It is noteworthy that the SBH of WC-*m*/WSe_2 heterostructures is exceptionally low, possibly due to a relatively substantial charge transfer ($0.21e$) from metal to WSe_2, resulting in Fermi levels closely approaching the CBM, thus leading to a very small SBH.

To quantify the difference between the SBH obtained from the pDOS and that derived from the ideal Schottky-Mott rule. We determined the work function of WC and the electron affinity of $WS(Se)_2$ separately under their isolated conditions. The work function of the WC [0001] surface is 5.08 eV for metal termination and 6.49 eV for carbon termination, belonging to high work function metals such as Au and Pd. The electron affinity of WS_2 and WSe_2 is 4.39 and 4.06 eV, respectively, which is consistent with previous computational work [56]. Following the Schottky-Mott rule formula,

$$\Phi_{\mathrm{SBH}} \approx \Phi_{\mathrm{metal}} - \chi_{\mathrm{semi}}, \tag{9}$$

where the Φ_{metal} and χ_{semi} are the work function of metals and the electron affinity of semiconductors. The SBH of four types of heterostructures are listed in Table VI. The results are much higher than that from pDOS, and also deviate from most of the data points in Fig. 8. For example, the SBH of WC-*c*/WS_2 is 94% larger than the results obtained from pDOS. Additionally, the SBH with WC-*c* is even greater than the band gap of semiconductors. This comparison underscores that the Schottky-Mott limit may not be applicable in our specific cases due to the presence of interfacial dipoles and charge redistribution.

V. CONCLUSIONS

In summary, by using the DFT method with van der Waals corrections, we investigated the geometric, energetic, and electronic properties of heterostructures between tungsten carbide and tungsten disulfide (diselenide). The Moiré pattern heterostructures are quantitatively proved to be energetically more favorable due to the large lattice mismatch between TMCs and TMDs. Through the comparison of the work of adhesion and interfacial energy, we determined the possible termination atoms of tungsten carbide, which may be difficult to observe through experimental characterization. The work of adhesion suggests that the weak van der Waals effect is the dominant effect between the interface, while the existing charge transfer accounts for the strong bonding characteristics. It is noted that the direction of charge transfer is opposite over the different termination, which results in the different types of major charge carriers. SBHs were quantitatively obtained by projected band structures and partial density of states. The WC-*c*/WSe_2 heterostructures possess the lowest SBH among the heterostructures considered. Our results thus provide insights into such novel heterostructures and are important for the designing and fabrication of novel electronic Schottky devices based on WS_2 and WSe_2.

ACKNOWLEDGMENT

This work was primarily supported by the Basic Office of Science of the Department of Energy under Award No. DE-SC0018025.

[1] K. S. Novoselov, A. K. Geim, S. V. Morozov, D. E. Jiang, Y. Zhang, S. V. Dubonos, I. V. Grigorieva, and A. A. Firsov, Electric field effect in atomically thin carbon films, Science **306**, 666 (2004).

[2] K. S. Novoselov, A. K. Geim, S. V. Morozov, D. Jiang, M. I. Katsnelson, I. V. Grigorieva, S. V. Dubonos, and A. A. Firsov, Two-dimensional gas of massless Dirac fermions in graphene, Nature (London) **438**, 197 (2005).

[3] A. C. Neto, F. Guinea, N. M. Peres, K. S. Novoselov, and A. K. Geim, The electronic properties of graphene, Rev. Mod. Phys. **81**, 109 (2009).

[4] Q. Tang and Z. Zhou, Graphene-analogous low-dimensional materials, Prog. Mater. Sci. **58**, 1244 (2013).

[5] K. Kostarelos and K. S. Novoselov, Graphene devices for life, Nat. Nanotechnol. **9**, 744 (2014).

[6] X. Wang and G. Shi, Flexible graphene devices related to energy conversion and storage, Energy Environ. Sci. **8**, 790 (2015).

[7] F. Wang, J. H. Gosling, G. F. Trindade, G. A. Rance, O. Makarovsky, N. D. Cottam, Z. Kudrynskyi, A. G. Balanov, M. T. Greenaway, R. D. Wildman, R. Hague, C. Tuck, T. M. Fromhold, and L. Turyanska, Inter-flake quantum transport of electrons and holes in inkjet-printed graphene devices, Adv. Funct. Mater. **31**, 2007478 (2021).

[8] A. Kareekunnan, T. Agari, A. M. Hammam, T. Kudo, T. Maruyama, H. Mizuta, and M. Muruganathan, Revisiting the mechanism of electric field sensing in graphene devices, ACS Omega **6**, 34086 (2021).

[9] J. Kang, W. Liu, D. Sarkar, D. Jena, and K. Banerjee, Computational study of metal contacts to monolayer transition-metal dichalcogenide semiconductors, Phys. Rev. X **4**, 031005 (2014).

[10] Y. Liu, P. Stradins, and S. H. Wei, Van der Waals metal-semiconductor junction: Weak Fermi level pinning enables effective tuning of Schottky barrier, Sci. Adv. **2**, e1600069 (2016).

[11] O. Mashtalir, M. Naguib, V. N. Mochalin, Y. Dall'Agnese, M. Heon, M. W. Barsoum, and Y. Gogotsi, Intercalation and delamination of layered carbides and carbonitrides, Nat. Commun. **4**, 1716 (2013).

[12] M. Ghidiu, M. R. Lukatskaya, M. Q. Zhao, Y. Gogotsi, and M. W. Barsoum, Conductive two-dimensional titanium carbide 'clay' with high volumetric capacitance, Nature (London) **516**, 78 (2014).

[13] J. Xu, J. Shim, J. H. Park, and S. Lee, MXene electrode for the integration of WSe_2 and MoS_2 field effect transistors, Adv. Funct. Mater. **26**, 5328 (2016).

[14] Q. Peng, C. Si, J. Zhou, and Z. Sun, Modulating the Schottky barriers in MoS_2/MXenes heterostructures via surface functionalization and electric field, Appl. Surf. Sci. **480**, 199 (2019).

[15] M. Li, Y. Xu, B. Zhao, C. Wu, Q. Zhou, Z. Wang, T. Li, and W. Ju, Exploration of electrical contact type in two-dimensional WS_2/Nb_2CX_2 (X = H, F, Cl) heterostructures, Appl. Surf. Sci. **602**, 154390 (2022).

[16] C. Li, J. Guo, C. Wang, D. Ma, and B. Wang, Design of MXene contacts for high-performance WS_2 transistors, Appl. Surf. Sci. **527**, 146701 (2020).

[17] C. Xu, L. Wang, Z. Liu, L. Chen, J. Guo, N. Kang, X.-L. Ma, H.-M. Cheng, and W. Ren, Large-area high-quality 2D ultrathin Mo_2C superconducting crystals, Nat. Mater. **14**, 1135 (2015).

[18] Z. Kang, Y. Cheng, Z. Zheng, F. Cheng, Z. Chen, L. Li, X. Tan, L. Xiong, and Y. Gao, MoS_2-based photodetectors powered by asymmetric contact structure with large work function difference, Nano-Micro Lett. **11**, 34 (2019).

[19] J. Jeon, Y. Park, S. Choi, J. Lee, S. S. Lim, B. H. Lee, Y. J. Song, J. H. Cho, Y. H. Jang, and S. Lee, Epitaxial synthesis of molybdenum carbide and formation of a Mo_2C/MoS_2 hybrid structure via chemical conversion of molybdenum disulfide, ACS Nano **12**, 338 (2018).

[20] S. Choi, Y. J. Kim, J. Jeon, B. H. Lee, J. H. Cho, and S. Lee, Scalable two-dimensional lateral metal/semiconductor junction fabricated with selective synthetic integration of transition-metal-carbide (Mo_2C)/-dichalcogenide (MoS_2), ACS Appl. Mater. Interfaces **11**, 47190 (2019).

[21] F. Zhang, W. Zheng, Y. Lu, L. Pabbi, K. Fujisawa, A. L. Elías, A. R. Binion, T. Granzier-Nakajima, T. Zhang, Y. Lei, Z. Lin, E. W. Hudson, S. B. Sinnott, L. Balicas, and M. Terrones, Superconductivity enhancement in phase-engineered molybdenum carbide/disulfide vertical heterostructures, Proc. Natl. Acad. Sci. USA **117**, 19685 (2020).

[22] X. Tang, L. Yang, J. Huang, W. Chen, B. Li, S. Yang, R. Yang, Z. Zeng, Z. Tang, and X. Gui, Controlling sulfurization of 2D Mo_2C crystal for Mo_2C/MoS_2-based memristor and artificial synapse, npj Flexible Electron. **6**, 93 (2022).

[23] W. Huang, H. Meng, Y. Gao, J. Wang, C. Yang, D. Liu, J. Liu, C. Guo, B. Yang, and W. Cao, Metallic tungsten carbide nanoparticles as a near-infrared-driven photocatalyst, J. Mater. Chem. A **7**, 18538 (2019).

[24] K. He, J. Xie, Z. Yang, R. Shen, Y. Fang, S. Ma, X. Chen, and X. Li, Earth-abundant WC nanoparticles as an active noble-metal-free co-catalyst for the highly boosted photocatalytic H_2 production over g-C_3N_4 nanosheets under visible light, Catal. Sci. Technol. **7**, 1193 (2017).

[25] J. S. Jang, D. J. Ham, N. Lakshminarasimhan, W. yong Choi, and J. S. Lee, Role of platinum-like tungsten carbide as cocatalyst of CdS photocatalyst for hydrogen production under visible light irradiation, Appl. Catal. A **346**, 149 (2008).

[26] S. L. Wang, Y. Zhu, X. Luo, Y. Huang, J. Chai, T. I. Wong, and G. Q. Xu, 2D WC/WO_3 heterogeneous hybrid for photocatalytic decomposition of organic compounds with Vis–NIR light, Adv. Funct. Mater. **28**, 1705357 (2018).

[27] C. Ren, W. Li, H. Li, X. Ma, X. Li, H. Fan, M. Dong, Y. Li, and N. Chen, Fabrication of chrysanthemum-like CdSe/bulk WC: A novel Schottky-junction photocatalyst for improving photocatalytic hydrogen production, J. Alloys Compd. **872**, 159691 (2021).

[28] Y. Lei, K. H. Ng, Y. Zhang, Z. Li, S. Xu, J. Huang, and Y. Lai, One-pot loading of cadmium sulfide onto tungsten carbide for efficient photocatalytic H_2 evolution under visible light irradiation, Chem. Eng. J. **434**, 134689 (2022).

[29] A. Fiori, T. Teraji, and Y. Koide, Thermal stabilization and deterioration of the WC/p-type diamond (100) Schottky-barrier interface, Physica Status Solidi A **211**, 2363 (2014).

[30] J. Hu, X. Jian, T. Yang, and X. Peng, Investigation on the interface characteristic between WC (001) and diamond (111) by first-principles calculation, Diamond Relat. Mater. **123**, 108864 (2022).

[31] G. Kresse and J. Furthmüller, Efficiency of ab-initio total energy calculations for metals and semiconductors using a plane-wave basis set, Comput. Mater. Sci. **6**, 15 (1996).

[32] G. Kresse and D. Joubert, From ultrasoft pseudopotentials to the projector augmented-wave method, Phys. Rev. B **59**, 1758 (1999).

[33] J. P. Perdew, K. Burke, and M. Ernzerhof, Generalized gradient approximation made simple, Phys. Rev. Lett. **77**, 3865 (1996).

[34] M. Dion, H. Rydberg, E. Schröder, D. C. Langreth, and B. I. Lundqvist, Van der Waals density functional for general geometries, Phys. Rev. Lett. **92**, 246401 (2004).

[35] V. Wang, N. Xu, J. C. Liu, G. Tang, and W. T. Geng, VASPKIT: A user-friendly interface facilitating high-throughput computing and analysis using VASP code, Comput. Phys. Commun. **267**, 108033 (2021).

[36] C. M. Fernandes and A. M. R. Senos, Cemented carbide phase diagrams: A review, Int. J. Refract. Met. Hard Mater. **29**, 405 (2011).

[37] C. Wang, L. Chen, Z. Liu, Z. Liu, X. L. Ma, C. Xu, H.-M. Cheng, W. Ren, and N. Kang, Transport properties of topological semimetal tungsten carbide in the 2D limit, Adv. Electron. Mater. **5**, 1800839 (2019).

[38] Y. Li, Y. Gao, B. Xiao, T. Min, Z. Fan, S. Ma, and D. Yi, Theoretical study on the electronic properties and stabilities of low-index surfaces of WC polymorphs, Comput. Mater. Sci. **50**, 939 (2011).

[39] X. Zhao, Y. Zhuo, S. Liu, Y. Zhou, C. Zhao, C. Wang, and Q. Yang, Investigation on WC/TiC interface relationship in wear-resistant coating by first-principles, Surf. Coat. Technol. **305**, 200 (2016).

[40] T. Björkman, A. Gulans, A. V. Krasheninnikov, and R. M. Nieminen, van der Waals bonding in layered compounds from advanced density-functional first-principles calculations, Phys. Rev. Lett. **108**, 235502 (2012).

[41] Z. Liu, A. Wang, P. Liu, and J. Xie, Investigation on the WC/Cu interfacial bonding properties: First-principles prediction and experimental verification, Int. J. Refract. Met. Hard Mater. **106**, 105872 (2022).

[42] L. Y. Gan, Y. J. Zhao, D. Huang, and U. Schwingenschlögl, First-principles analysis of MoS_2/Ti_2C and MoS_2/Ti_2CY_2 (Y = F and OH) all-2D semiconductor/metal contacts, Phys. Rev. B **87**, 245307 (2013).

[43] P. C. Shen *et al.*, Ultralow contact resistance between semimetal and monolayer semiconductors, Nature (London) **593**, 211 (2021).

[44] Q. Wang, L. Cao, S. J. Liang, W. Wu, G. Wang, C. H. Lee, W. L. Ong, H. Y. Yang, L. K. Ang, S. A. Yang, and Y. S. Ang, Efficient Ohmic contacts and built-in atomic sublayer protection in $MoSi_2N_4$ and WSi_2N_4 monolayers, npj 2D Mater. Appl. **5**, 71 (2021).

[45] J. G. Simmons, Generalized formula for the electric tunnel effect between similar electrodes separated by a thin insulating film, J. Appl. Phys. **34**, 1793 (1963).

[46] T. Su, Y. Li, Q. Wang, W. Zhao, L. Cao, and Y. S. Ang, Semimetal contacts to monolayer semiconductor: Weak metalization as an effective mechanism to Schottky barrier lowering, J. Phys. D: Appl. Phys. **56**, 234001 (2023).

[47] W. Ai, Y. Shi, X. Hu, J. Yang, and L. Sun, Tunable Schottky barrier and efficient Ohmic contacts in MSi_2N_4 (M = Mo, W)/2D metal contacts, ACS Appl. Electron. Mater. **5**, 5606 (2023).

[48] V. Sorkin, H. Zhou, Z. G. Yu, K. W. Ang, and Y. W. Zhang, The effects of point defect type, location, and density on the Schottky barrier height of Au/MoS_2 heterojunction: A first-principles study, Sci. Rep. **12**, 18001 (2022).

[49] B. Liu, L. J. Wu, Y. Q. Zhao, L. Z. Wang, and M.-Q. Cai, First-principles investigation of the Schottky contact for the two-dimensional MoS_2 and graphene heterostructure, RSC Adv. **6**, 60271 (2016).

[50] Y. Wang, M. Ye, M. Weng, J. Li, X. Zhang, H. Zhang, Y. Guo, Y. Pan, L. Xiao, J. Liu, F. Pan, and J. Lu, Electrical contacts in monolayer arsenene devices, ACS Appl. Mater. Interfaces **9**, 29273 (2017).

[51] H. Tang, B. Shi, Y. Pan, J. Li, X. Zhang, J. Yan, S. Liu, J. Yang, L. Xu, J. Yang, M. Wu, and J. Lu, Schottky contact in monolayer WS_2 field-effect transistors, Adv. Theory Simul. **2**, 1900001 (2019).

[52] L. Yao, J. Yun, P. Kang, H. Zhao, J. Yan, W. Zhao, and Z. Zhang, Electronic properties, interface contact and transport properties of strain-modulated MS_2/borophosphene and MSeS/borophosphene (M = Cr, Mo, W) heterostructure: Insights from first-principles, Appl. Surf. Sci. **652**, 159363 (2024).

[53] R. T. Tung, The physics and chemistry of the Schottky barrier height, Appl. Phys. Rev. **1**, 011304 (2014).

[54] K. Sotthewes, R. Van Bremen, E. Dollekamp, T. Boulogne, K. Nowakowski, D. Kas, H. J. W. Zandvliet, and P. Bampoulis, Universal Fermi-level pinning in transition-metal dichalcogenides, J. Phys. Chem. C **123**, 5411 (2019).

[55] Y. Guo, D. Liu, and J. Robertson, 3D behavior of Schottky barriers of 2D transition-metal dichalcogenides, ACS Appl. Mater. Interfaces **7**, 25709 (2015).

[56] H. G. Kim and H. J. Choi, Thickness dependence of work function, ionization energy, and electron affinity of Mo and W dichalcogenides from DFT and GW calculations, Phys. Rev. B **103**, 085404 (2021).